© 2020. Published by The Company of Biologists Ltd | Journal of Experimental Biology (2020) 223, jeb227108. doi:10.1242/jeb.227108

METHODS & TECHNIQUES

A coordinate-system-independent method for comparing joint rotational mobilities

Armita R. Manafzadeh* and Stephen M. Gatesy

ABSTRACT

Three-dimensional studies of range of motion currently plot joint poses in a 'Euler space' whose axes are angles measured in the joint's three rotational degrees of freedom. Researchers then compute the volume of a pose cloud to measure rotational mobility. However, pairs of poses that are equally different from one another in orientation are not always plotted equally far apart in Euler space. This distortion causes a single joint's mobility to change when measured based on different joint coordinate systems and precludes fair comparison among joints. Here, we present two alternative spaces inspired by a 16th century map projection – cosine-corrected and sine-corrected Euler spaces – that allow coordinate-system-independent comparison of joint rotational mobility. When tested with data from a bird hip joint, cosine-corrected Euler space demonstrated a 10-fold reduction in variation among mobilities measured from three joint coordinate systems. This new quantitative framework enables previously intractable, comparative studies of articular function.

KEY WORDS: Mobility, Range of motion, Euler angles, Joint coordinate system, XROMM, Visualization

INTRODUCTION

Many studies aim to quantify joint rotational mobility in both extant and extinct animals (e.g. Arnold et al., 2014; Hutson and Hutson, 2012, 2013, 2014, 2015, 2017, 2018; Kambic et al., 2017a; Pierce et al., 2012; Proffen et al., 2012; Taylor and Wedel, 2013) and humans (e.g. Diong et al., 2019; Matthews et al., 2017; McGarry et al., 2016; Mulholland and Wyss, 2001; Steinberg et al., 2016). These studies have traditionally reported range of motion (ROM) with bar graphs displaying the minimum and maximum excursions possible in each of a joint's rotational degrees of freedom (DoF). However, recent work has highlighted substantial interactions among DoF (e.g. Haering et al., 2014; Kambic et al., 2017b), motivating the development of a method to visualize and measure ROM in three dimensions (3D) (Crétual et al., 2015; Haering et al., 2014; Kambic et al., 2017b; Manafzadeh and Padian, 2018; Ropars et al., 2015).

After calculating a series of Tait–Bryan (i.e. extrinsic *XYZ*, *XZY*, *YXZ*, *YZX*, *ZXY*, *ZYX*) or proper Euler (i.e. extrinsic *XYX*, *XZX*, *YXY*, *YZY*, *ZXZ*, *ZYZ*) angles from a joint coordinate system (JCS), researchers plot a point representing each joint pose in a 3D 'Euler space' whose axes are angles (α, β and γ) measured in the three DoF of the JCS rotation sequence. This process is repeated for hundreds or thousands of joint poses, creating a point cloud that offers a visual representation of a joint's ROM. A convex hull (Crétual et al., 2015; Haering et al., 2014; Kambic et al., 2017b; Ropars et al., 2015) or other alpha shape (Manafzadeh and Padian, 2018; Tonneau et al., 2014) can then be calculated and its volume measured to quantify mobility. Although plotting in Euler space is fairly new to biomechanists, this approach has been used by other researchers studying 3D orientations, such as materials scientists and molecular biologists, for several decades (e.g. Bailor et al., 2011; Cho et al., 2004; Dickson et al., 2014; Flowers, 1983; Houtte, 1987; Raabe, 1995).

Unfortunately, pairs of joint poses that are equally different from one another in orientation are rarely plotted equally far apart in Euler space (see Data Table 1 in Dryad: https://doi.org/10.5061/dryad.dncjsxkx1). For example, under Tait–Bryan rotation conventions, poses of equal difference fall out farther and farther away from each other as the second rotation (β) approaches ±90° (i.e. as the system approaches gimbal lock). A useful intuition for this distortion can be developed by drawing an analogy between a Tait–Bryan JCS and the geographic coordinate system on the surface of the Earth (following Baker, 2011; Strasser, 1917). Consider a globe turned on its side with a bird femur spanning a radius from center (hip joint) to equator (condyles). Following the avian hip JCS proposed by Kambic et al. (2014), rotation about the first JCS axis (generally, α; here, flexion–extension) moves the distal femur to a new line of longitude. Rotation about the second axis (generally, β; here, abduction–adduction) moves the femur to a new line of latitude. Finally, rotation about the third axis (generally, γ; here, long-axis rotation) spins the femoral condyles in place as if setting a new navigational heading (Fig. 1A–D).

If the distal femur begins on the prime meridian at an adducted, equatorial latitude (Pose 1), and the hip extends to a longitude of 20°W (Pose 2), the femur must travel 2226 km along the surface of the Earth, making Poses 1 and 2 rather different (Fig. 1E). However, longitude lines converge as they approach the poles – so if the distal femur begins on the prime meridian at a more abducted, Arctic latitude (e.g. 70°N; Pose 3) and the hip is again extended to a longitude of 20°W (Pose 4), the femur only travels 761 km and Poses 3 and 4 are much more similar (Fig. 1F). Problematically, the distances between Poses 1 and 2 and Poses 3 and 4 are identical in Euler space (Fig. 1H). In order for the femur to travel 2226 km at a latitude of 70°N (i.e. to reach a pose as different from Pose 3 as Pose 2 is from Pose 1), the hip must extend to the significantly greater longitude of 58°W (Pose 5; Fig. 1G). In Euler space, Pose 5 is plotted almost 3× farther away from Pose 3 than Pose 2 is from Pose 1 (Fig. 1H). A pair of equally different poses at an extremely abducted, northern Greenlandic latitude of 80°N – even closer to the pole – would be plotted almost 6× farther apart.

Department of Ecology and Evolutionary Biology, Brown University, Providence, RI 02912, USA.

*Author for correspondence (armita_manafzadeh@brown.edu)

A.R.M., 0000-0001-5388-7942; S.M.G., 0000-0003-1701-0320

Received 17 April 2020; Accepted 29 July 2020

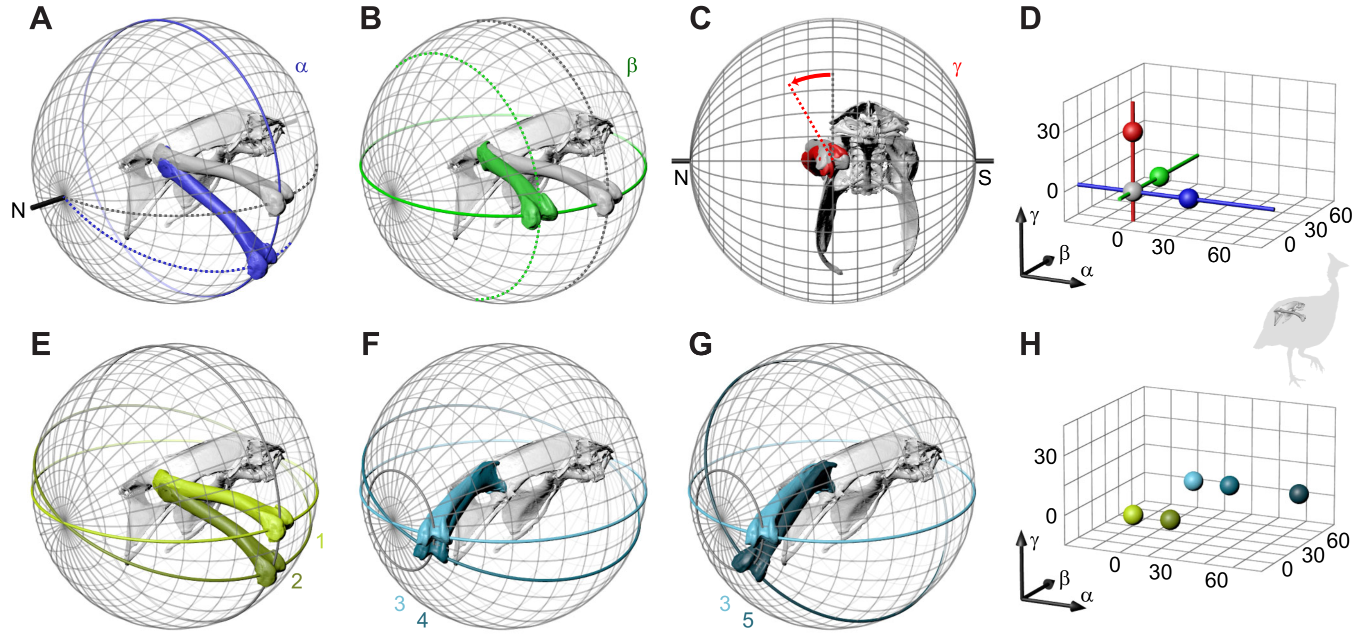

Fig. 1. An analogy between a Tait–Bryan joint coordinate system (JCS) and the geographical coordinate system underscores the shortcomings of Euler space. Poses of a guineafowl's right hip joint are represented both on globes (rotated 90 deg such that the North Pole faces left; A–C,E–G) and in Euler space (D,H). Inset shows the position of the pelvis and right femur within a silhouette of the helmeted guineafowl (*Numida meleagris*). (A) Rotation about the first JCS axis (generally, α; here, flexion–extension) moves the distal femur to a new line of longitude. (B) Rotation about the second axis (generally, β; here, abduction–adduction) moves the femur to a new line of latitude. (C) Rotation about the third axis (generally, γ; here, long-axis rotation) spins the femoral condyles in place as if setting a new navigational heading. (D) Excursions in any one degree of freedom (DoF; α, β or γ) correspond to motions along one axis of Euler space. (E) Poses 1 and 2, differing in 20° of longitude at the equator, are rather different. (F) Poses 3 and 4, differing in 20° of longitude at an Arctic latitude, are quite similar. (G) To reach a pose as different from Pose 3 as Pose 1 is from Pose 2, the hip must extend to a significantly more westerly longitude. (H) Poses 1–5 plotted in Euler space (colors match those in E–G). Note that poses 3 and 5 are plotted much farther apart than poses 1 and 2 are.

If the hip joint were instead measured using a different JCS, this invisible globe would be reoriented, and all poses would move closer to or farther from the poles of the system. As a result, analyses of joint mobility in Euler space depend heavily on a researcher's selection of a JCS, because this choice determines where along the second axis of the space a pose cloud will be plotted – and thus how big its volume will be (see a discussion of related issues in Michaud et al., 2012; Šenk and Chèze, 2006). In other words, the same set of joint poses, when plotted in Euler space based on two different JCSs, can yield two very different mobility measurements. A related issue plagues comparisons among two or more joints, even when all are analyzed using the same JCS. Volumes of pose clouds that deviate farther from zero along the second axis will be disproportionately inflated, causing the joints being compared to appear more similar or more different than they truly are.

Here, we present two alternative spaces for plotting joint poses and comparing joint rotational mobility: a 'cosine-corrected Euler space' for use with any Tait–Bryan rotation convention, and a 'sine-corrected Euler space' for use with any proper Euler rotation convention. Plots in these spaces represent all poses of equal difference at equal distances, meaning that mobility calculations are resistant to changes in the JCS selected. Therefore, our method enables accurate comparative studies of articular function.

MATERIALS AND METHODS

Cosine-corrected and sine-corrected Euler spaces

In order to devise a coordinate-system-independent method for comparing joint mobility, we first sought to better understand the pattern of volume distortion throughout Euler space. Conveniently, doing so requires only a basic knowledge of calculus. An expression for a volume element (dV; the volume of an infinitesimally small region of a space) can be computed by finding the determinant of the Jacobian matrix for the transformation from a 3D Euler parametrization to 4D quaternionic space (where dV is standard; see Karney, 2007) and taking the absolute value of its inverse. We calculated the volume element for a generalized Tait–Bryan rotation convention and obtained $dV=8/\mathrm{abs}[\cos(\beta)]d\alpha d\beta d\gamma$, and for a generalized proper Euler rotation convention and obtained $dV=8/\mathrm{abs}[\sin(\beta)]d\alpha d\beta d\gamma$ (see Appendix). These calculations revealed that volumes measured in any Euler space are distorted by a surprisingly simple trigonometric function (Tait–Bryan: 1/cosine=secant; proper Euler: 1/sine=cosecant) of the second rotation.

The volume element is generally used to integrate multivariate functions. However, because joint pose data are empirically derived, we aimed to harness this expression to create a 3D space that does not distort volumes but still permits fast, easy visualizations of poses and measurements of mobility. Given the analogy between Tait–Bryan angles and the geographic coordinate system, we turned to the cartographic literature for inspiration – and found a serendipitous solution in a 1570 map of the world drawn by Jean Cossin de Dieppe (Fig. 2A). Cossin's map is based on a projection first developed by Gerardus Mercator and known today as the sinusoidal (SIN) or Sanson–

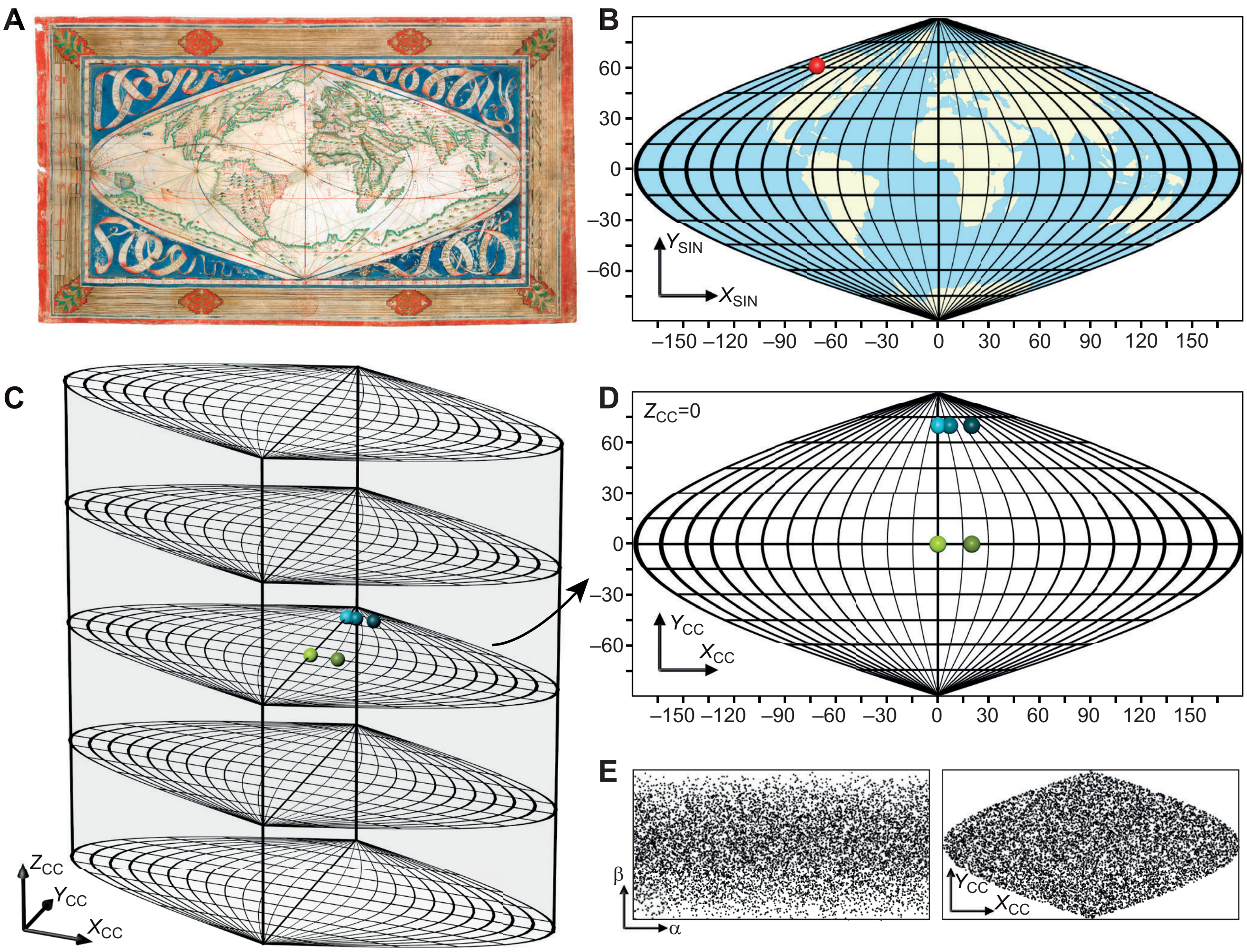

Fig. 2. A 16th century map projection is the foundation of cosine-corrected Euler space. (A) Jean Cossin de Dieppe's 1570 map of the world (source: Bibliothèque Nationale de France). (B) Anchorage, AK, USA, plotted on a sinusoidal map projection (Source: Gaba, Wikimedia Commons). (C) Poses 1–5 (colors match those in Fig. 1H) plotted in cosine-corrected Euler space. (D) A focused view of Poses 1–5 in cosine-corrected Euler space; note that Poses 1 and 2 and Poses 3 and 5 are plotted equally far apart from each other. (E) When viewed from above, 10,000 uniformly random poses plotted in a Tait–Bryan Euler space (left) are unevenly distributed, but become evenly dense when plotted in cosine-corrected Euler space (right).

Flamsteed equal-area map projection, which is defined by:

$$X_{SIN} = (\lambda - \lambda_0)\cos(\varphi), \tag{1}$$

$$Y_{SIN} = \varphi, \tag{2}$$

where λ is longitude, λ_0 is the longitude of the prime meridian and ϕ is latitude (Seong et al., 2002). For example, Anchorage, AK, USA, sits on the globe at roughly 61°N, 150°W [i.e. (λ, ϕ)=(−150, 61)], and is plotted as (X_{SIN}, Y_{SIN})=(−72, 61) (Fig. 2B). By including a cosine term, the sinusoidal projection corrects for meridional (longitudinal) convergence on the surface of the Earth and does not distort areas.

Building from the definition of the sinusoidal map projection, we created what we call 'cosine-corrected (CC) Euler space', defined by:

$$X_{CC} = (\alpha - \alpha_{central})\cos(\beta), \tag{3}$$

$$Y_{CC} = \beta, \tag{4}$$

$$Z_{CC} = \gamma, \tag{5}$$

where, when measured under a Tait–Bryan rotation convention, α is the angle measured about the first JCS axis in the rotation sequence, $\alpha_{central}$ is the α value centered in the space (analogous to the prime meridian), β is the angle measured about the second JCS axis in the rotation sequence, and γ is the angle measured about the third JCS axis in the rotation sequence. For example, when $\alpha_{central}$=0, Pose 4 (see Fig. 1F,H) – measured as (α, β, γ)=(20, 70, 0) – is plotted as (X_{CC}, Y_{CC}, Z_{CC})=(7, 70, 0) (Fig. 2C,D). If the canonical set of Euler triples where α ϵ (−180, 180), β ϵ (−90, 90) and γ ϵ (−180, 180) is selected, cosine-corrected Euler space takes the form of a sinusoidal map projection extruded into and out of the plane of the page (Fig. 2C). NB: $\alpha_{central}$ is arbitrary and can be altered, as long as the set of Euler triples used is shifted accordingly [e.g. $\alpha_{central}$=90 requires α ϵ (−90 to 270)]. As we would expect from the value of the Tait–Bryan volume element, this space plots all poses of equal difference at equal distances (Fig. 2E; see Data Table 1 in Dryad: https://doi.org/10.5061/dryad.dncjsxkx1; see also Kuffner, 2004) and does not distort volumes.

Similarly, then, we created what we call 'sine-corrected (SC) Euler space', defined by:

$$X_{SC} = (\alpha - \alpha_{central})\sin(\beta), \tag{6}$$

$$Y_{SC} = \beta, \tag{7}$$

$$Z_{SC} = \gamma, \tag{8}$$

for use with joints measured using a proper Euler rotation convention (e.g. human shoulders; Wu et al., 2005). If the canonical set of Euler triples where $\alpha \in (-180, 180)$, $\beta \in (-180, 0)$ and $\gamma \in (-180, 180)$ is selected, sine-corrected Euler space superficially resembles cosine-corrected Euler space. And once again, as we would expect from the value of the proper Euler volume element, this space plots all poses of equal difference at equal distances (see Data Table 1 in Dryad: https://doi.org/10.5061/dryad.dncjsxkx1) and does not distort volumes.

Sample joint ROM analysis

A fresh-frozen adult helmeted guineafowl, *Numida meleagris* (Linnaeus 1758), cadaver was obtained from colleagues (no approval from the Brown University Institutional Animal Care and Use Committee was necessary). Radiopaque markers (three per bone; 0.8 mm diameter zirconium oxide ball bearings; Ortech, Inc., Sacramento, CA, USA) were press-fitted into hand-drilled holes in the pelvis and right femur and affixed with cyanoacrylate adhesive. (The other hindlimb elements were also marked; these data are not presented here.) Care was taken to ensure minimal damage to hindlimb soft tissues, and all incisions were sutured after marker implantation.

The specimen was mounted in the center of an X-ray volume created by a pair of X-ray image systems (Imaging Systems and Service, Painesville, OH, USA) comprising Varian model G-1086 X-ray tubes and Dunlee model TH9447QXH590 image intensifiers in the W. M. Keck Foundation XROMM Facility at Brown University (70–85 kV, 200 mA, 120–122 cm source–image distance). To allow a researcher to conduct manipulations from a safe distance outside the X-ray volume, one or two 1.0 m wooden dowels were fastened to the marked hindlimb using Velcro and elastic bands. Biplanar fluoroscopic videos of the hip joint taken through its full ROM were recorded using Phantom v.10 high-speed cameras (50 frames s^{-1}, 1/1000 shutter speed, 100–150 µs EDR, 1760×1760 pixel resolution; Vision Research, Wayne, NJ, USA). Extremes of rotation were determined based on researcher sensation of a hard stop (following Kambic et al., 2017a,b; Manafzadeh and Padian, 2018). We recorded multiple trials to ensure the most complete sampling possible. Still X-ray images of a standard grid and an object of known geometry were also captured to allow undistortion and 3D calibration of the cameras (Knörlein et al., 2016).

Following video data collection, the specimen was disarticulated and micro-computed tomography scans were taken of the pelvis and right femur (115 kV, 130 µA, 0.090 mm slice thickness,

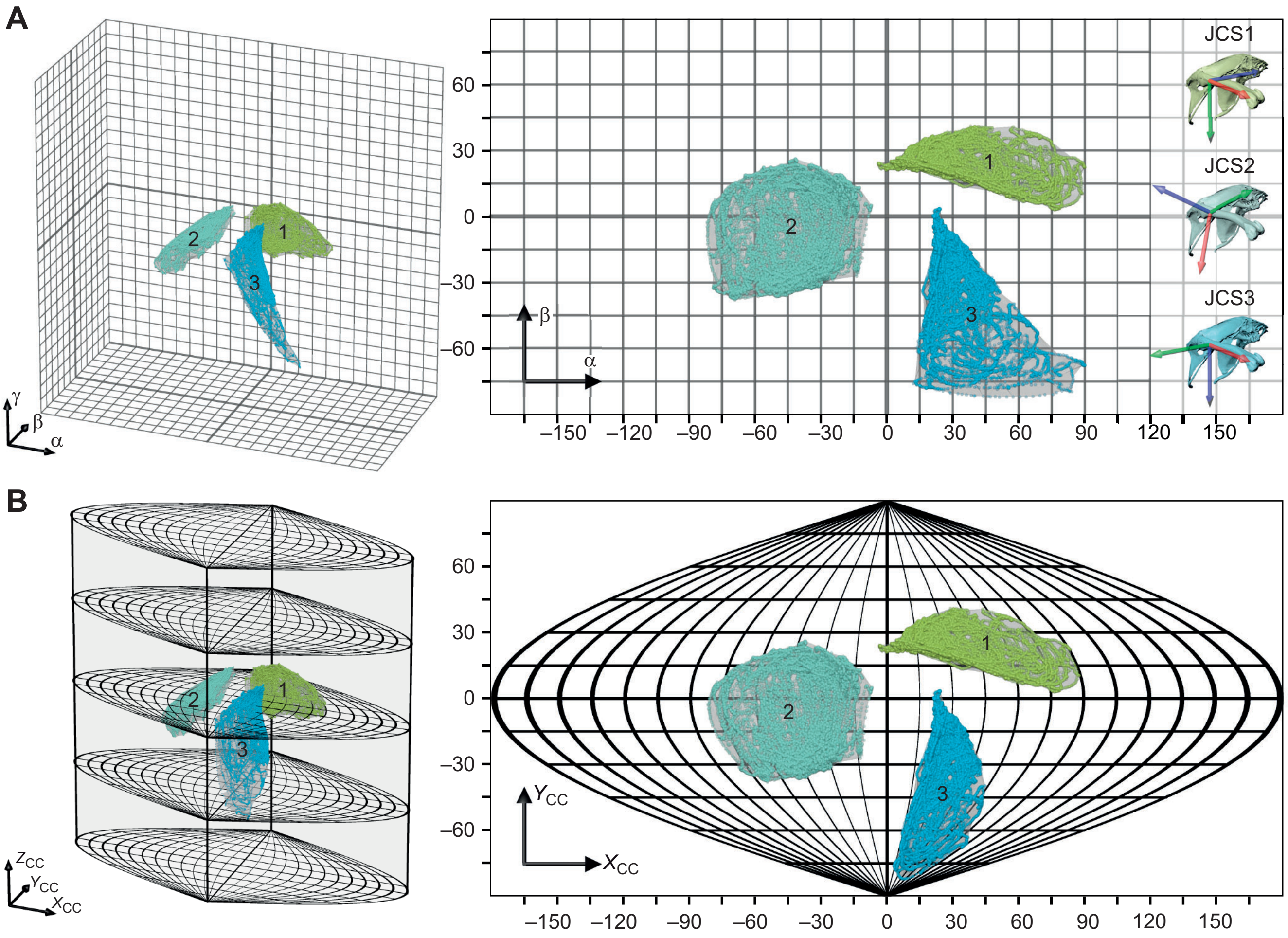

Fig. 3. Helmeted guineafowl hip poses plotted in Euler space and cosine-corrected Euler space. (A) Pose clouds and alpha shapes measured from JCS1–3 plotted in Euler space. Oblique view and top view. (B) Pose clouds and alpha shapes measured from JCS1–3 plotted in cosine-corrected Euler space. Oblique view and top view. Colors match those in A. All pose clouds contain 25,192 poses. See also Movie 1.

2000×2000 resolution; Nikon Xtek microCT, Nikon Metrology, Tokyo, Japan). Mesh models of bones and radiopaque markers were reconstructed using Amira v.6.0.1 (Mercury Systems, Andover, MA, USA) and cleaned using Geomagic Wrap 2017 (3D Systems, Morrisville, NC, USA). Models were imported into Maya 2020 (Autodesk, San Rafael, CA, USA), and three alternative sets of JCSs were placed at the hip joint (see Fig. 3A), here termed JCS1, JCS2 and JCS3.

X-ray videos were calibrated and digitized using XMALab v.1.5.4 (Knörlein et al., 2016); the overall precision of tracking was 0.106 mm (mean s.d. of intermarker distance for six co-osseous marker pairs over 14 trials; see Brainerd et al., 2010). Rigid body transformations were computed and used to animate bone models in Maya 2020, where joint rotations were calculated from JCS1–3 using the oRel XROMM shelf tool (xromm.org) under a Tait–Bryan *ZYX* rotation convention. This process yielded 25,192 measured hip joint poses for each JCS (see Data Table 2 in Dryad: https://doi.org/10.5061/dryad.dncjsxkx1).

We first plotted the three resulting pose clouds in Euler space and computed the volume of an alpha shape for each in MATLAB_R2019a (Mathworks, Natick, MA, USA), using either an alpha radius of 10 or the critical alpha radius if it was larger than 10 (see Table S1 for a sensitivity analysis). We then transformed all pose clouds to cosine-corrected Euler space and repeated our volumetric analysis.

RESULTS AND DISCUSSION

To test the effectiveness of our method on real physiological data, we compared the mobilities measured from a helmeted guineafowl hip joint using three different Tait–Bryan JCSs in both Euler space and cosine-corrected Euler space (Movie 1). In Euler space, we measured a mobility of 46,830 deg^3 using JCS1; 45,602 deg^3 using JCS2; and 65,260 deg^3 using JCS3 (Fig. 3A). In cosine-corrected Euler space, we measured a mobility of 43,033 deg^3 using JCS1; 43,208 deg^3 using JCS2; and 41,899 deg^3 using JCS3 (Fig. 3B). Whereas the largest percent difference in mobility was 30.12% in Euler space, cosine-corrected Euler space reduced this metric to only 3.03%.

The remaining discrepancy among mobilities stems from variation in the wrapping of the alpha shape for each point cloud – a limitation inherent to this volume measurement approach. Future studies might consider implementing more involved algorithms for computing volumes from pose sets (e.g. Luo et al., 2009), but in the meantime, alpha shapes continue to offer a convenient method for quantifying mobility. When alpha shapes are used, care should be taken to sample joint poses as densely as possible, because sparse pose clouds exacerbate wrapping discrepancies (see Table S2 for a sensitivity analysis).

We are by no means the first researchers to attempt to create a uniform space of 3D orientations. Scientists in other fields have previously developed methods that rely on quaternions (e.g. Krakow et al., 2017), Rodrigues vectors (e.g. Neumann, 1991), the Hopf fibration (e.g. Yershova et al., 2010) and even Euler angles (e.g. Zhao and Adams, 1988) (see Schwartz et al., 2009, for an overview). However, our approach is unique because we aimed to maintain a low mathematical barrier to use while balancing our dual goals of visualization and quantification. Consequently, a key advantage of cosine-corrected and sine-corrected Euler spaces for studying joints is their straightforward connection to the Euler-based JCSs that are recommended by the International Society of Biomechanics (Wu et al., 2002, 2005) and are so frequently used in 3D kinematic studies (see Brainerd et al., 2010). Simple trigonometry can transform each point in our spaces back into the original Euler triple that was measured from a JCS, minimizing the gap between abstract pose space and concrete morphological relationship.

We suggest that cosine-corrected and sine-corrected Euler spaces can be applied to a broad range of future studies, especially as 3D measurements of joint poses become increasingly common. For example, when measured in these spaces, the effects of injury (e.g. Lopes et al., 2016; Modest et al., 2019; Verrall et al., 2005), disease (e.g. Mitchell et al., 2019; Pratt and Ball, 2016; Srivanitchapoom et al., 2016) or soft tissue constraints (e.g. Arnold et al., 2014; Hutson and Hutson, 2012; Manafzadeh and Padian, 2018) on ROM can be judged fairly. And because mobility metrics in these spaces are coordinate-system independent, it is now feasible to investigate the development or evolution of mobility across disparate joints. Ultimately, the quantitative framework presented here corrects the volume distortion of Euler space and enables accurate comparative analyses of articular function.

APPENDIX

Computation of the volume element for the Tait–Bryan parametrization

To compute the volume element dV, we begin with the transformation from a generalized Tait–Bryan parametrization to quaternions where α is the first angle measured in the rotation sequence, β is the second angle measured in the rotation sequence and γ is the third angle measured in the rotation sequence. In order to obtain a square Jacobian (allowing computation of the determinant, which is only defined for square matrices), we temporarily include the radius term r, which we will set equal to 1 at the end of our calculations because we are only concerned with unit quaternions:

$$q_r = r\left(\cos\frac{\alpha}{2}\cos\frac{\beta}{2}\cos\frac{\gamma}{2} + \sin\frac{\alpha}{2}\sin\frac{\beta}{2}\sin\frac{\gamma}{2}\right), \tag{A1}$$

$$q_i = r\left(\sin\frac{\alpha}{2}\cos\frac{\beta}{2}\cos\frac{\gamma}{2} - \cos\frac{\alpha}{2}\sin\frac{\beta}{2}\sin\frac{\gamma}{2}\right), \tag{A2}$$

$$q_j = r\left(\cos\frac{\alpha}{2}\sin\frac{\beta}{2}\cos\frac{\gamma}{2} + \sin\frac{\alpha}{2}\cos\frac{\beta}{2}\sin\frac{\gamma}{2}\right), \tag{A3}$$

$$q_k = r\left(\cos\frac{\alpha}{2}\cos\frac{\beta}{2}\sin\frac{\gamma}{2} - \sin\frac{\alpha}{2}\sin\frac{\beta}{2}\cos\frac{\gamma}{2}\right). \tag{A4}$$

The Jacobian matrix is thus:

$$\begin{bmatrix}
\cos\frac{\gamma}{2}\cos\frac{\beta}{2}\cos\frac{\alpha}{2}+\sin\frac{\gamma}{2}\sin\frac{\beta}{2}\sin\frac{\alpha}{2} & -r\left(\frac{\sin\frac{\gamma}{2}\cos\frac{\beta}{2}\cos\frac{\alpha}{2}-\cos\frac{\gamma}{2}\sin\frac{\beta}{2}\sin\frac{\alpha}{2}}{2}\right) & -r\left(\frac{\cos\frac{\gamma}{2}\sin\frac{\beta}{2}\cos\frac{\alpha}{2}-\sin\frac{\gamma}{2}\cos\frac{\beta}{2}\sin\frac{\alpha}{2}}{2}\right) & -r\left(\frac{\cos\frac{\gamma}{2}\cos\frac{\beta}{2}\sin\frac{\alpha}{2}-\sin\frac{\gamma}{2}\sin\frac{\beta}{2}\cos\frac{\alpha}{2}}{2}\right) \\
\cos\frac{\gamma}{2}\cos\frac{\beta}{2}\sin\frac{\alpha}{2}-\sin\frac{\gamma}{2}\sin\frac{\beta}{2}\cos\frac{\alpha}{2} & -r\left(\frac{\cos\frac{\gamma}{2}\sin\frac{\beta}{2}\cos\frac{\alpha}{2}+\sin\frac{\gamma}{2}\cos\frac{\beta}{2}\sin\frac{\alpha}{2}}{2}\right) & -r\left(\frac{\sin\frac{\gamma}{2}\cos\frac{\beta}{2}\cos\frac{\alpha}{2}+\cos\frac{\gamma}{2}\sin\frac{\beta}{2}\sin\frac{\alpha}{2}}{2}\right) & r\left(\frac{\cos\frac{\gamma}{2}\cos\frac{\beta}{2}\cos\frac{\alpha}{2}+\sin\frac{\gamma}{2}\sin\frac{\beta}{2}\sin\frac{\alpha}{2}}{2}\right) \\
\cos\frac{\gamma}{2}\sin\frac{\beta}{2}\cos\frac{\alpha}{2}+\sin\frac{\gamma}{2}\cos\frac{\beta}{2}\sin\frac{\alpha}{2} & r\left(\frac{\cos\frac{\gamma}{2}\cos\frac{\beta}{2}\sin\frac{\alpha}{2}-\sin\frac{\gamma}{2}\sin\frac{\beta}{2}\cos\frac{\alpha}{2}}{2}\right) & r\left(\frac{\cos\frac{\gamma}{2}\cos\frac{\beta}{2}\cos\frac{\alpha}{2}-\sin\frac{\gamma}{2}\sin\frac{\beta}{2}\sin\frac{\alpha}{2}}{2}\right) & r\left(\frac{\sin\frac{\gamma}{2}\cos\frac{\beta}{2}\cos\frac{\alpha}{2}-\cos\frac{\gamma}{2}\sin\frac{\beta}{2}\sin\frac{\alpha}{2}}{2}\right) \\
\sin\frac{\gamma}{2}\cos\frac{\beta}{2}\cos\frac{\alpha}{2}-\cos\frac{\gamma}{2}\sin\frac{\beta}{2}\sin\frac{\alpha}{2} & r\left(\frac{\cos\frac{\gamma}{2}\cos\frac{\beta}{2}\cos\frac{\alpha}{2}+\sin\frac{\gamma}{2}\sin\frac{\beta}{2}\sin\frac{\alpha}{2}}{2}\right) & -r\left(\frac{\cos\frac{\gamma}{2}\cos\frac{\beta}{2}\sin\frac{\alpha}{2}+\sin\frac{\gamma}{2}\sin\frac{\beta}{2}\cos\frac{\alpha}{2}}{2}\right) & -r\left(\frac{\cos\frac{\gamma}{2}\sin\frac{\beta}{2}\cos\frac{\alpha}{2}+\sin\frac{\gamma}{2}\cos\frac{\beta}{2}\sin\frac{\alpha}{2}}{2}\right)
\end{bmatrix}$$

Taking the inverse of the absolute value of the determinant of this matrix yields:

$$\frac{8}{|\cos\beta| \times |r^3|}.$$

Substituting 1 for r, dV is:

$$\frac{8}{|\cos\beta|}\,\mathrm{d}\alpha\;\;\mathrm{d}\beta\;\;\mathrm{d}\gamma.$$

Computation of the volume element for the proper Euler parametrization

Computation of the volume element dV for the proper Euler parametrization follows that for the Tait–Bryan parametrization. The transformation from a generalized proper Euler parametrization to quaternions is:

$$q_r = r\left(\cos\frac{\alpha+\gamma}{2}\cos\frac{\beta}{2}\right), \tag{A5}$$

$$q_i = r\left(\cos\frac{\alpha-\gamma}{2}\sin\frac{\beta}{2}\right), \tag{A6}$$

$$q_j = r\left(\sin\frac{\alpha-\gamma}{2}\sin\frac{\beta}{2}\right), \tag{A7}$$

$$q_k = r\left(\sin\frac{\alpha+\gamma}{2}\cos\frac{\beta}{2}\right). \tag{A8}$$

The Jacobian matrix is thus:

$$\begin{bmatrix}
\cos\frac{\beta}{2}\sin\frac{\gamma+\alpha}{2} & -\frac{r}{2}\left(\cos\frac{\beta}{2}\sin\frac{\gamma+\alpha}{2}\right) & -\frac{r}{2}\left(\sin\frac{\beta}{2}\cos\frac{\gamma+\alpha}{2}\right) & -\frac{r}{2}\left(\cos\frac{\beta}{2}\sin\frac{\gamma+\alpha}{2}\right) \\
\sin\frac{\beta}{2}\sin\frac{\gamma-\alpha}{2} & -\frac{r}{2}\left(\sin\frac{\beta}{2}\sin\frac{\gamma-\alpha}{2}\right) & \frac{r}{2}\left(\cos\frac{\beta}{2}\cos\frac{\gamma-\alpha}{2}\right) & \frac{r}{2}\left(\sin\frac{\beta}{2}\sin\frac{\gamma-\alpha}{2}\right) \\
-\sin\frac{\beta}{2}\sin\frac{\gamma-\alpha}{2} & -\frac{r}{2}\left(\sin\frac{\beta}{2}\cos\frac{\gamma-\alpha}{2}\right) & -\frac{r}{2}\left(\cos\frac{\beta}{2}\sin\frac{\gamma-\alpha}{2}\right) & \frac{r}{2}\left(\sin\frac{\beta}{2}\cos\frac{\gamma-\alpha}{2}\right) \\
\cos\frac{\beta}{2}\sin\frac{\gamma+\alpha}{2} & \frac{r}{2}\left(\cos\frac{\beta}{2}\cos\frac{\gamma+\alpha}{2}\right) & -\frac{r}{2}\left(\sin\frac{\beta}{2}\sin\frac{\gamma+\alpha}{2}\right) & \frac{r}{2}\left(\cos\frac{\beta}{2}\cos\frac{\gamma+\alpha}{2}\right)
\end{bmatrix}$$

Taking the inverse of the absolute value of the determinant of this matrix yields:

$$\frac{8}{|\sin\beta| \times |r^3|}.$$

Substituting 1 for r, dV is:

$$\frac{8}{|\sin\beta|}\,\mathrm{d}\alpha\;\;\mathrm{d}\beta\;\;\mathrm{d}\gamma$$

Acknowledgements

The authors thank David Baier for the XROMM_MayaTools; Karyn Roorda and John Hermanson for the helmeted guineafowl specimen; Peter Bishop, Eva Herbst, John 'Spike' Hughes, James Kuffner, David Laidlaw, Shoeleh Mutameni, Morgan Turner and Madhusudhan Venkadesan for conversations that greatly improved the quality of the manuscript; and two anonymous reviewers for their helpful feedback.

Competing interests

The authors declare no competing or financial interests.

Author contributions

Conceptualization: A.R.M., S.M.G.; Methodology: A.R.M., S.M.G.; Software: A.R.M., S.M.G.; Validation: A.R.M., S.M.G.; Formal analysis: A.R.M., S.M.G.; Investigation: A.R.M., S.M.G.; Resources: A.R.M., S.M.G.; Data curation: A.R.M., S.M.G.; Writing - original draft: A.R.M., S.M.G.; Writing - review & editing: A.R.M., S.M.G.; Visualization: A.R.M., S.M.G.; Supervision: S.M.G.; Project administration: S.M.G.; Funding acquisition: A.R.M.

Funding

This work was supported by a National Science Foundation Graduate Research Fellowship, a Brown University Presidential Fellowship, a Sigma Xi Grant-in-Aid of Research, a Society of Vertebrate Paleontology Cohen Award for Student Research, a Winifred Goldring Award from the Association for Women Geoscientists and the Paleontological Society, and a Bushnell Graduate Research and Education Fund Award to A.R.M.

Data availability

Data are available from the Dryad Digital Repository (Manafzadeh and Gatesy, 2020): dryad.dncjsxkx1.

Supplementary information

Supplementary information available online at
https://jeb.biologists.org/lookup/doi/10.1242/jeb.227108.supplemental

References

Arnold, P., Fischer, M. S. and Nyakatura, J. A. (2014). Soft tissue influence on ex vivo mobility in the hip of Iguana: comparison with in vivo movement and its bearing on joint motion of fossil sprawling tetrapods. *J. Anat.* **225**, 31-41. doi:10.1111/joa.12187

Bailor, M. H., Mustoe, A. M., Brooks, C. L., , III and Al-Hashimi, H. M. (2011). 3D maps of RNA interhelical junctions. *Nat. Protoc.* **6**, 1536. doi:10.1038/nprot.2011.385

Baker, R. (2011). Globographic visualisation of three dimensional joint angles. *J. Biomech.* **44**, 1885-1891. doi:10.1016/j.jbiomech.2011.04.031

Brainerd, E. L., Baier, D. B., Gatesy, S. M., Hedrick, T. L., Metzger, K. A., Gilbert, S. L. and Crisco, J. J. (2010). X-ray reconstruction of moving morphology (XROMM): precision, accuracy and applications in comparative biomechanics research. *J. Exp. Zool. A Ecol. Genet. Physiol.* **313**, 262-279. doi:10.1002/jez.589

Cho, J.-H., Rollett, A. D. and Oh, K. H. (2004). Determination of volume fractions of texture components with standard distributions in Euler space. *Metallurg. Mater. Trans. A* **35**, 1075-1086. doi:10.1007/s11661-004-1010-y

Crétual, A., Bonan, I. and Ropars, M. (2015). Development of a novel index of shoulder's mobility based on the configuration space volume and its link to mono-axial amplitudes. *Man. Ther.* **20**, 433-439. doi:10.1016/j.math.2014.10.020

Dickson, A., Mustoe, A. M., Salmon, L. and Brooks, C. L., III (2014). Efficient in silico exploration of RNA interhelical conformations using Euler angles and WExplore. *Nucleic Acids Res.* **42**, 12126-12137. doi:10.1093/nar/gku799

Diong, J., Gandevia, S. C., Nguyen, D., Foo, Y., Kastre, C., Andersson, K., Butler, J. E. and Héroux, M. E. (2019). Small amounts of involuntary muscle activity reduce passive joint range of motion. *J. Appl. Physiol.* **127**, 229-234. doi:10.1152/japplphysiol.00168.2019

Flowers, J. W. (1983). Volume fractions of texture components of cubic materials. *Textures Microstruct.* **5**, 820640. doi:10.1155/TSM.5.205

Haering, D., Raison, M. and Begon, M. (2014). Measurement and description of three-dimensional shoulder range of motion with degrees of freedom interactions. *J. Biomech. Eng.* **136**, 084502. doi:10.1115/1.4027665

Houtte, P. V. (1987). On the representation of texture functions of cubic metals in Euler space. *Textures Microstruct.* **7**, 187-205. doi:10.1155/TSM.7.187

Hutson, J. D. and Hutson, K. N. (2012). A test of the validity of range of motion studies of fossil archosaur elbow mobility using repeated-measures analysis and the extant phylogenetic bracket. *J. Exp. Biol.* **215**, 2030-2038. doi:10.1242/jeb.069567

Hutson, J. D. and Hutson, K. N. (2013). Using the American alligator and a repeated-measures design to place constraints on in vivo shoulder joint range of motion in dinosaurs and other fossil archosaurs. *J. Exp. Biol.* **216**, 275-284. doi:10.1242/jeb.074229

Hutson, J. D. and Hutson, K. N. (2014). A repeated–measures analysis of the effects of soft tissues on wrist range of motion in the extant phylogenetic bracket of dinosaurs: Implications for the functional origins of an automatic wrist folding mechanism in crocodilia. *Anat. Rec.* **297**, 1228-1249. doi:10.1002/ar.22903

Hutson, J. D. and Hutson, K. N. (2015). Inferring the prevalence and function of finger hyperextension in A rchosauria from finger–joint range of motion in the A merican alligator. *J. Zool.* **296**, 189-199. doi:10.1111/jzo.12232

Hutson, J. D. and Hutson, K. N. (2017). An investigation of the locomotor function of therian forearm pronation provides renewed support for an arboreal, chameleon-like evolutionary stage. *J. Mamm. Evol.* **24**, 159-177. doi:10.1007/s10914-016-9341-1

Hutson, J. D. and Hutson, K. N. (2018). Retention of the flight-adapted avian finger-joint complex in the Ostrich helps identify when wings began evolving in dinosaurs. *Ostrich* **89**, 173-186. doi:10.2989/00306525.2017.1422566

Kambic, R. E., Roberts, T. J. and Gatesy, S. M. (2014). Long-axis rotation: a missing degree of freedom in avian bipedal locomotion. *J. Exp. Biol.* **217**, 2770-2782. doi:10.1242/jeb.101428

Kambic, R. E., Biewener, A. A. and Pierce, S. E. (2017a). Experimental determination of three-dimensional cervical joint mobility in the avian neck. *Front. Zool.* **14**, 37. doi:10.1186/s12983-017-0223-z

Kambic, R. E., Roberts, T. J. and Gatesy, S. M. (2017b). 3–D range of motion envelopes reveal interacting degrees of freedom in avian hind limb joints. *J. Anat.* **231**, 906-920. doi:10.1111/joa.12680

Karney, C. F. F. (2007). Quaternions in molecular modeling. *J. Mol. Graph. Model.* **25**, 595-604. doi:10.1016/j.jmgm.2006.04.002

Knörlein, B. J., Baier, D. B., Gatesy, S. M., Laurence-Chasen, J. D. and Brainerd, E. L. (2016). Validation of XMALab software for marker-based XROMM. *J. Exp. Biol.* **219**, 3701-3711. doi:10.1242/jeb.145383

Krakow, R., Bennett, R. J., Johnstone, D. N., Vukmanovic, Z., Solano-Alvarez, W., Lainé, S. J., Einsle, J. F., Midgley, P. A., Rae, C. M. F. and Hielscher, R. (2017). On three-dimensional misorientation spaces. *Proc. R. Soc. A Math. Phys. Eng. Sci.* **473**, 20170274. doi:10.1098/rspa.2017.0274

Lopes, O. V., Gomes, J. L. E. and de Freitas Spinelli, L. (2016). Range of motion and radiographic analysis of the hip in patients with contact and non-contact anterior cruciate ligament injury. *Knee Surg. Sports Traumatol. Arthroscopy* **24**, 2868-2873. doi:10.1007/s00167-015-3532-9

Luo, C., Sun, J. and Wang, Y. (2009). Integral estimation from point cloud in d-dimensional space: a geometric view. In Proceedings of the Twenty-Fifth Annual Symposium on Computational Geometry, pp. 116-124.

Manafzadeh, A. R. and Padian, K. (2018). ROM mapping of ligamentous constraints on avian hip mobility: implications for extinct ornithodirans. *Proc. R. Soc. B* **285**, 20180727. doi:10.1098/rspb.2018.0727

Manafzadeh, A. R. and Gatesy, S. M. (2020). Data for: A coordinate-system-independent method for comparing joint rotational mobilities, v3, Dryad, Dataset. https://doi.org/10.5061/dryad.dncjsxkx1

Matthews, M. J., Green, D., Matthews, H. and Swanwick, E. (2017). The effects of swimming fatigue on shoulder strength, range of motion, joint control, and performance in swimmers. *Phys. Ther. Sport* **23**, 118-122. doi:10.1016/j.ptsp.2016.08.011

McGarry, M. H., Nguyen, M. L., Quigley, R. J., Hanypsiak, B., Gupta, R. and Lee, T. Q. (2016). The effect of long and short head biceps loading on glenohumeral joint rotational range of motion and humeral head position. *Knee Surg. Sports Traumatol. Arthroscopy* **24**, 1979-1987. doi:10.1007/s00167-014-3318-5

Michaud, B., Jackson, M. I., Prince, F. and Begon, M. S. (2012). Can one angle be simply subtracted from another to determine range of motion in three-dimensional motion analysis? *Comput. Methods Biomech. Biomed. Engin.* **17**, 507-515. doi:10.1080/10255842.2012.696104

Mitchell, T., Conradsson, D. and Paquette, C. (2019). Gait and trunk kinematics during prolonged turning in Parkinson's disease with freezing of gait. *Parkinson. Relat. Disorders* **64**, 188-193. doi:10.1016/j.parkreldis.2019.04.011

Modest, J., Clair, B., DeMasi, R., Meulenaere, S., Howley, A., Aubin, M. and Jones, M. (2019). Self-measured wrist range of motion by wrist-injured and wrist-healthy study participants using a built-in iPhone feature as compared with a universal goniometer. *J. Hand Ther.* **32**, 507-514. doi:10.1016/j.jht.2018.03.004

Mulholland, S. J. and Wyss, U. P. (2001). Activities of daily living in non-Western cultures: range of motion requirements for hip and knee joint implants. *Int. J. Rehabil. Res.* **24**, 191-198. doi:10.1097/00004356-200109000-00004

Neumann, P. (1991). Graphical representations of orientations and ODFs by Rodrigues vectors. *Steel Res.* **62**, 560-566. doi:10.1002/srin.199100450

Pierce, S. E., Clack, J. A. and Hutchinson, J. R. (2012). Three-dimensional limb joint mobility in the early tetrapod Ichthyostega. *Nature* **486**, 523-526. doi:10.1038/nature11124

Pratt, A. L. and Ball, C. (2016). What are we measuring? A critique of range of motion methods currently in use for Dupuytren's disease and recommendations for practice. *BMC Musculoskelet. Disord.* **17**, 20. doi:10.1186/s12891-016-0884-3

Proffen, B. L., McElfresh, M., Fleming, B. C. and Murray, M. M. (2012). A comparative anatomical study of the human knee and six animal species. *Knee* **19**, 493-499. doi:10.1016/j.knee.2011.07.005

Raabe, D. (1995). Textures of strip cast and hot rolled ferritic and austenitic stainless steel. *Mater. Sci. Technol.* **11**, 461-468. doi:10.1179/mst.1995.11.5.461

Ropars, M., Cretual, A., Thomazeau, H., Kaila, R. and Bonan, I. (2015). Volumetric definition of shoulder range of motion and its correlation with clinical signs of shoulder hyperlaxity. A motion capture study. *J. Shoulder Elbow Surg.* **24**, 310-316. doi:10.1016/j.jse.2014.06.040

Schwartz, A. J., Kumar, M., Adams, B. L. and Field, D. P. (eds.) (2009). *Electron Backscatter Diffraction in Materials Science*, Vol. 2, pp. 35-52. New York: Springer.

Šenk, M. and Chèze, L. (2006). Rotation sequence as an important factor in shoulder kinematics. *Clin. Biomech.* **21**, S3-S8. doi:10.1016/j.clinbiomech.2005.09.007

Seong, J. C., Mulcahy, K. A. and Usery, E. L. (2002). The sinusoidal projection: A new importance in relation to global image data. *Professional Geographer* **54**, 218-225. doi:10.1111/0033-0124.00327

Srivanitchapoom, P., Shamim, E. A., Diomi, P., Hattori, T., Pandey, S., Vorbach, S., Park, J. E., Wu, T., Auh, S. and Hallett, M. (2016). Differences in active range of motion measurements in the upper extremity of patients with writer's cramp compared with healthy controls. *J. Hand Ther.* **29**, 489-495. doi:10.1016/j.jht.2016.02.001

Steinberg, N., Hershkovitz, I., Zeev, A., Rothschild, B. and Siev-Ner, I. (2016). Joint hypermobility and joint range of motion in young dancers. *J. Clin. Rheumatol.* **22**, 171-178. doi:10.1097/RHU.0000000000000420

Strasser, H. (1917). *Lehrbuch der Muskel-und Gelenkmechanik*, Vol. III, Berlin: J. Springer.

Taylor, M. P. and Wedel, M. J. (2013). The effect of intervertebral cartilage on neutral posture and range of motion in the necks of sauropod dinosaurs. *PLoS ONE* **8**, e78214. doi:10.1371/journal.pone.0078214

Tonneau, S., Pettré, J. and Multon, F. (2014). Using task efficient contact configurations to animate creatures in arbitrary environments. *Comput. Graphics* **45**, 40-50. doi:10.1016/j.cag.2014.08.005

Verrall, G. M., Hamilton, I. A., Slavotinek, J. P., Oakeshott, R. D., Spriggins, A. J., Barnes, P. G. and Fon, G. T. (2005). Hip joint range of motion reduction in sports-related chronic groin injury diagnosed as pubic bone stress injury. *J. Sci. Med. Sport* **8**, 77-84. doi:10.1016/S1440-2440(05)80027-1

Wu, G., Siegler, S., Allard, P., Kirtley, C., Leardini, A., Rosenbaum, D., Whittle, M., D'Lima, D. D., Cristofolini, L., Witte, H. et al. (2002). ISB recommendation on definitions of joint coordinate system of various joints for the reporting of human joint motion—part I: ankle, hip, and spine. *J. Biomech.* **35**, 543-548. doi:10.1016/S0021-9290(01)00222-6

Wu, G., van der Helm, F. C. T., Veeger, H. E. J. D., Makhsous, M., Van Roy, P., Anglin, C., Nagels, J., Karduna, A. R., McQuade, K., Wang, X. et al. (2005). ISB recommendation on definitions of joint coordinate systems of various joints for the reporting of human joint motion—Part II: shoulder, elbow, wrist and hand. *J. Biomech.* **38**, 981-992. doi:10.1016/j.jbiomech.2004.05.042

Yershova, A., Jain, S., Lavalle, S. M. Mitchell, J. C. (2010). Generating uniform incremental grids on SO (3) using the Hopf fibration. *Int. J. Robot. Res.* **29**, 801-812. doi:10.1177/0278364909352700

Zhao, J. and Adams, B. L. (1988). Definition of an asymmetric domain for intercrystalline misorientation in cubic materials in the space of Euler angles. *Acta Crystallogr. Sec. A Found. Crystallogr.* **44**, 326-336. doi:10.1107/S010876738701256X